Supplement of Nat. Hazards Earth Syst. Sci., 24, 163–177, 2024
https://doi.org/10.5194/nhess-24-163-2024-supplement

Natural Hazards and Earth System Sciences
Open Access
EGU

Supplement of

Update on the seismogenic potential of the Upper Rhine Graben southern region

Sylvain Michel et al.

Correspondence to: Sylvain Michel (sylvain_michel@live.fr)

Contents of this file

Text S1 to S2

Figures S1 to S19

S1: Declustering from Marsan et al. (2017)

Marsan et al. (2017) approach for declustering is based on the space-time Epidemic-Type Aftershock Sequence (ETAS) model (Ogata, 1998). We first estimate M_c by fitting the magnitude frequency distribution (MFD) of earthquakes by the following model (Ogata and Katsura, 1993; Daniel et al., 2008): $N(m) = A \times 10^{-bm} \times q(m)$. $N(m)$ is the number of events of magnitude m, $q(m)$ corresponds to the probability of an event of magnitude m to occur during the time period of the analyzed catalog, b corresponds to the b-value of the MFD, and A is a constant. Events below the maximum curvature, roughly indicating M_c (Wiemer and Wyss, 2000), are also included in the fit. $q(m)$ is defined by Ogata and Katsura (1993) equation:

$$q(m) = \frac{1}{2} + \frac{1}{2}\ erf(\frac{m - \mu}{\sqrt{2\sigma}})$$

where erf is the error function. The parameters μ, σ, b, and A are evaluated from the data and M_c is estimated using $M_c = \mu + 2\,\sigma$ (i.e. with 97.7% confidence). The declustering of the catalog for events above M_c is done using the same parametrization as Jara et al. (2017). M_c is estimated at 2.2 and 3.2 for the instrumental (>1994) and historical (>1850) catalogs. The results of the declustering of the instrumental and historical catalogs are shown in Figure S7 and S8.

S2: Declustering from Zaliapin & Ben Zion (2013)

We use the declustering method of Zaliapin and Ben-Zion (2013) with the same catalogs and magnitude of completeness as for Marsan et al. (2017) (Section 3.2 in main text and Text S1). The parameters for Zaliapin and Ben-Zion (2013) method include two parameters to be tuned: the fractal dimension of epicenters that we chose equal to 1.6, the default value used by Zaliapin and Ben-Zion (2013) in southern California; and the b-value. We tested three different b-values (0.5, 1.0 and 1.5). The results of the declustering are shown in Figure S13 and S14, and its impact on the probabilities of M_{max}, the b-value and $P(\tau \mid M_w = M_{Mode})$ are shown in Figure S15. The three different b-values tested provide very similar results (Figure S15).

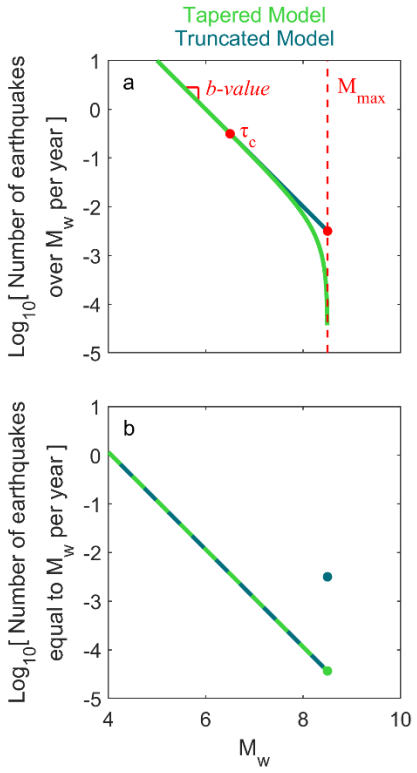

Figure S1: Illustration of the tapered and the truncated models in their (a) cumulative form and (b) non-cumulative form. M_{max}, the recurrence time of events of a certain magnitude (τ_c), and the b-value indicate the three parameters that control those models.

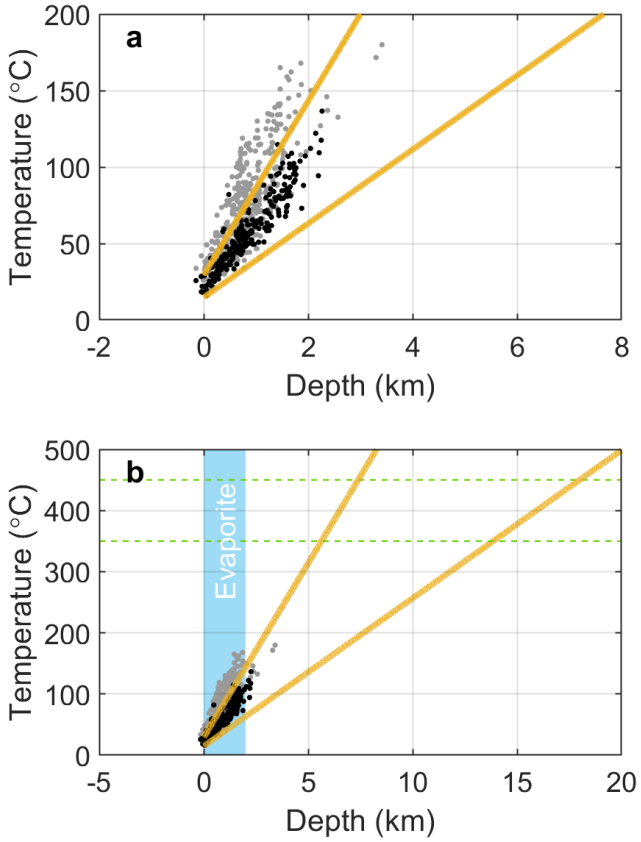

Figure S2: (a) Temperature as a function of depth based on borehole data from Guillou-Frottier et al. (2013) (grey dots). The black dots indicate the borehole data south of the city of Strasbourg, within the region of interest. The envelope of the black dots is roughly indicated by the yellow lines. (b) Same as (a) but with larger depth and temperature ranges. The dashed green horizontal lines indicate the 350°C and 450°C isotherms, between which a transition in frictional properties occurs for quartzo-feldspathic rocks (Blanpied et al., 1995). The blue shaded area highlights the potential depth range for the potash-salt evaporitic basin.

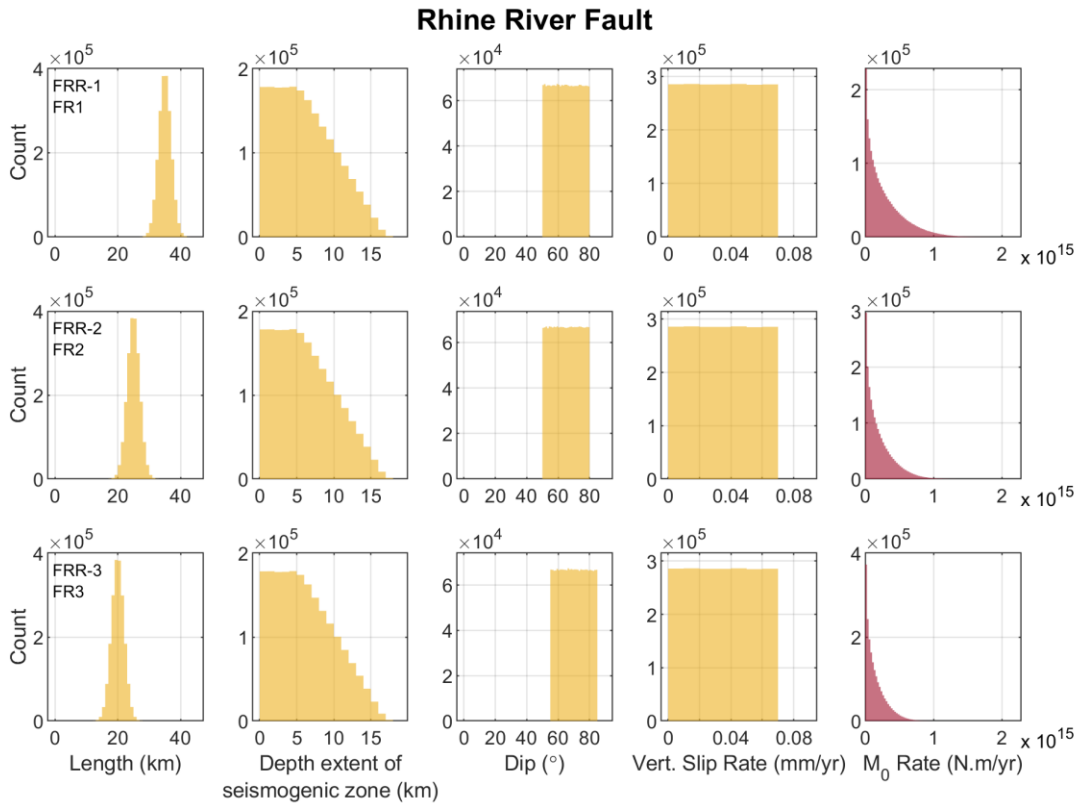

Figure S3: Constitutive parameter PDFs of each segment of the Rhine River Fault. Note that the samples are identical for each segment for the depth extent of the seismogenic zone and for the vertical slip rate. The details of the PDFs are given in Table 1.

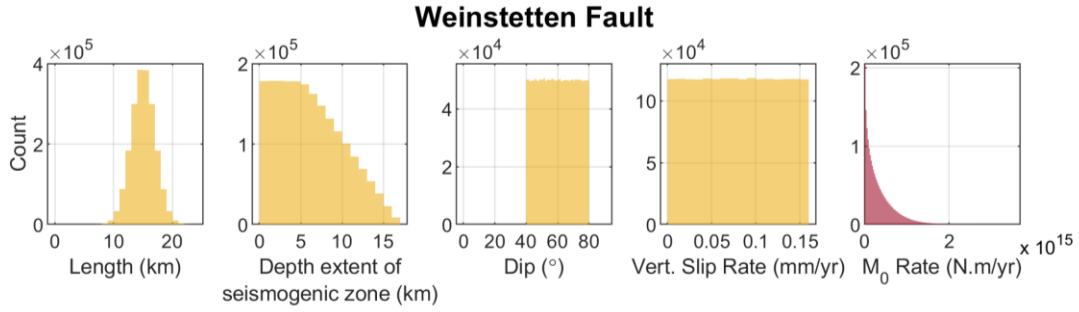

Figure S4: Same as Figure S3 but for the Weinstetten Fault.

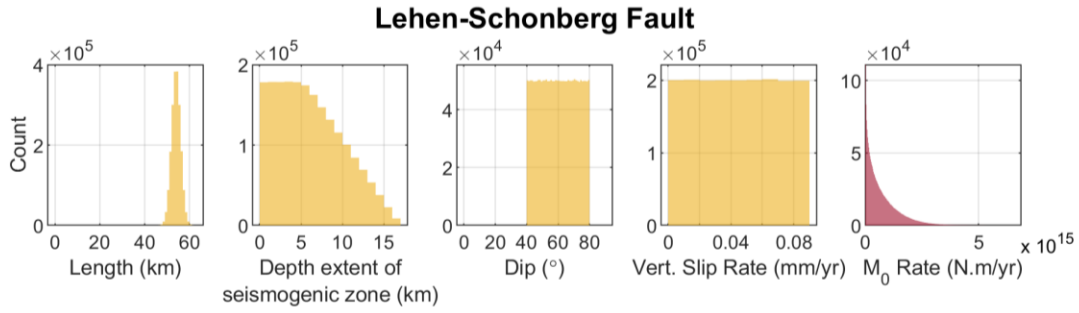

Figure S5: Same as Figure S3 but for the Lehen-Schonberg Fault.

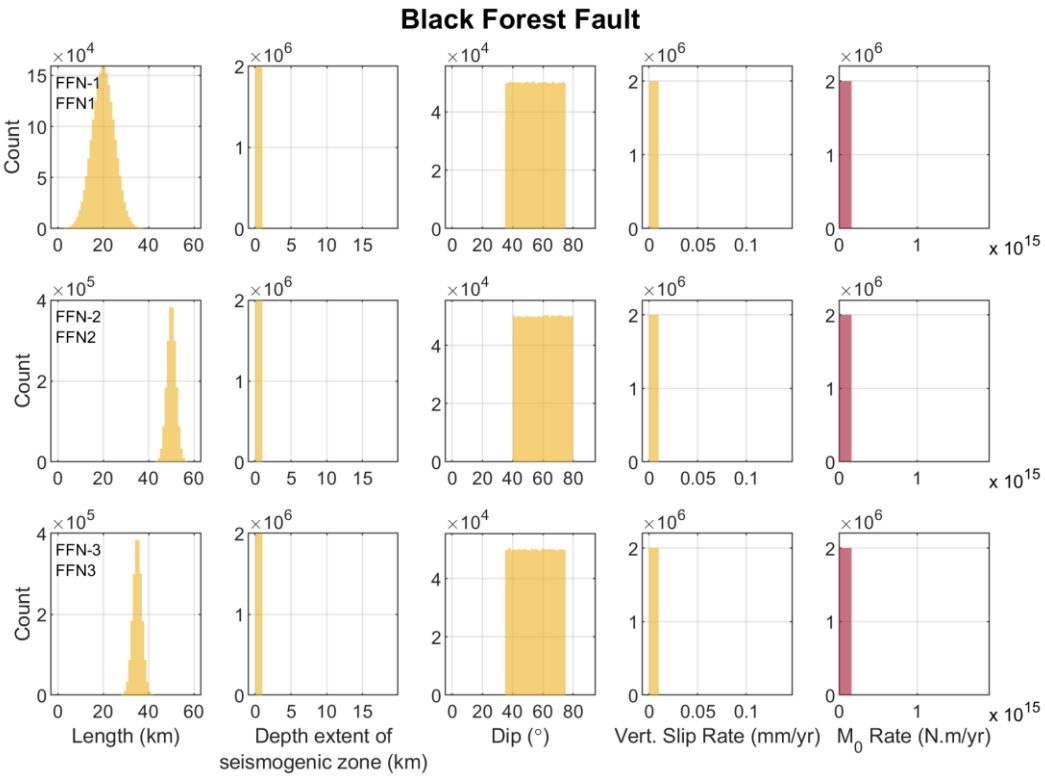

Figure S6: Same as Figure S3 but for the Black Forest Fault.

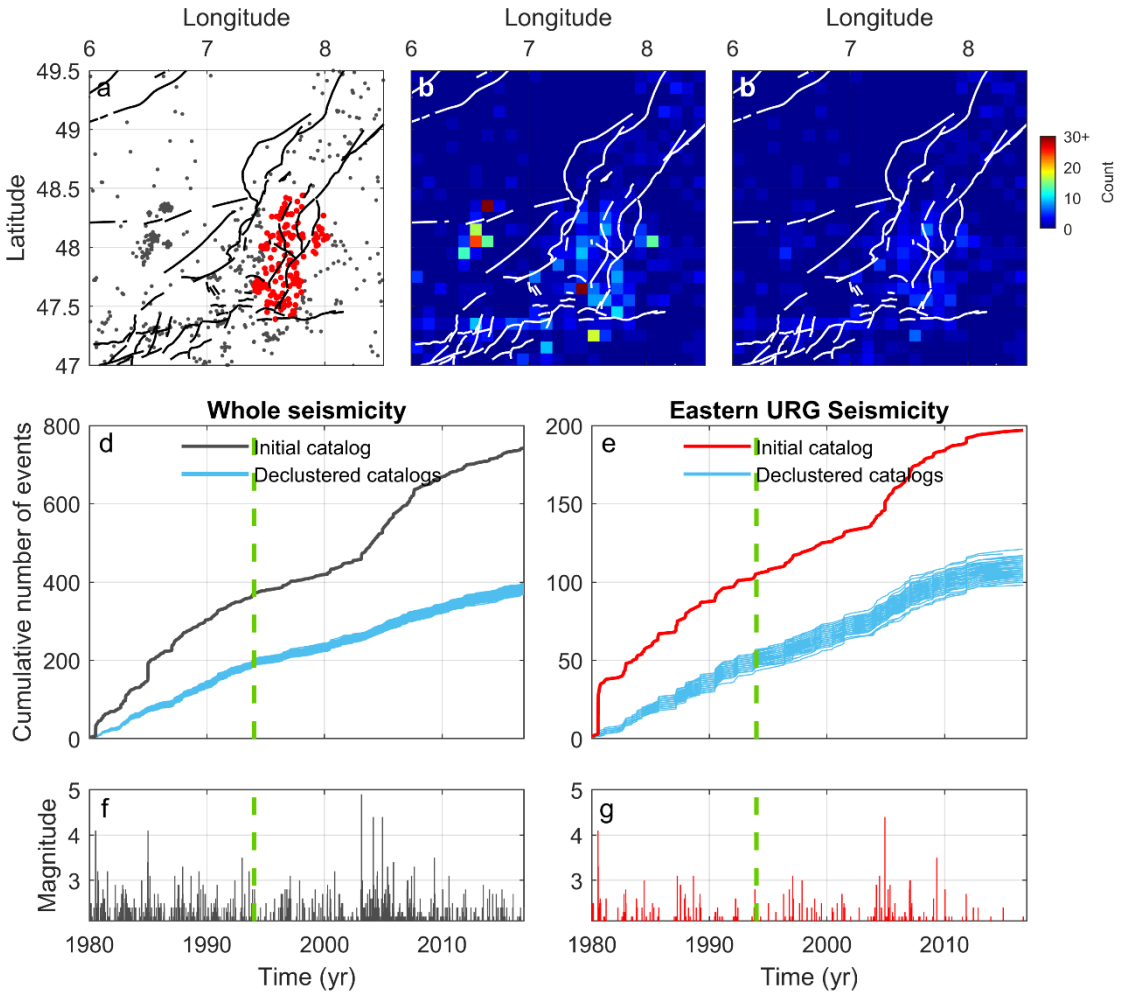

Figure S7: (a) Seismicity in the southern Upper Rhine Graben region from Drouet et al.'s (2020) catalog between 1980 and 2016 ($M_c = 2.2$). Events represented with red dots indicate the ones selected for the seismic potential analysis. (b) Earthquake density map with $M_w \geq 2.2$. (c) Background earthquake density map from the declustering of events with $M_w \geq 2.2$ (Marsan et al., 2017). The number of earthquakes per cell (0.1° x 0.1° in longitude and latitude) indicates the mean number of events based on 100 catalogs created from sampling, for each event, the probability of being part of background seismicity. (d) Cumulative number of events since 1980 using the whole earthquake catalog. The grey and blue curves indicate the results before and after declustering, respectively. One hundred declustered catalogs are shown to illustrate the effect of sampling the probability of events to be mainshocks. The dashed green vertical line indicates the date from which we assume the catalog to be complete. (e) Same as (d) but for the selected events (red dots in (a)). (f) and (g) show the magnitude of the events over time for the whole catalog and for the selected events.

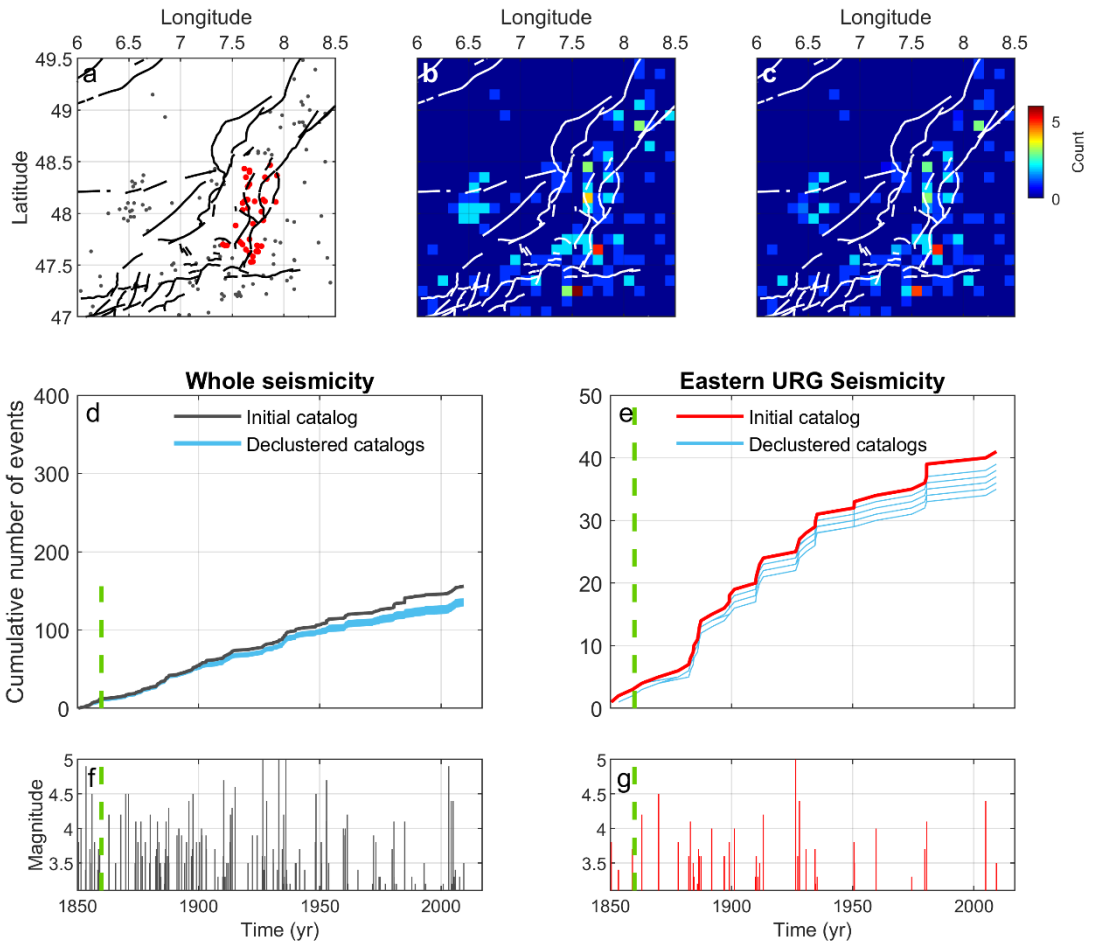

Figure S8: Same as Figure S7 but for the period between 1850 and 2016, taking $M_c = 3.2$.

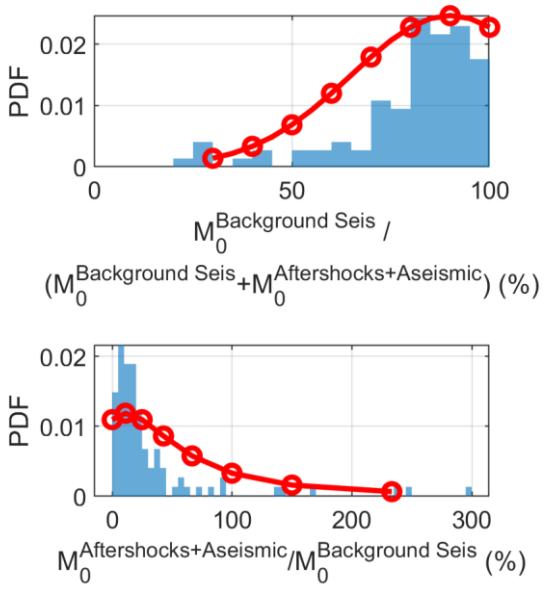

Figure S9: Afterslip and aftershock contribution. Blue histograms are based on Churchill et al. (2022) dataset. The red lines and dots correspond to the PDFs used and values explored for the seismicity models in Section 3.3.

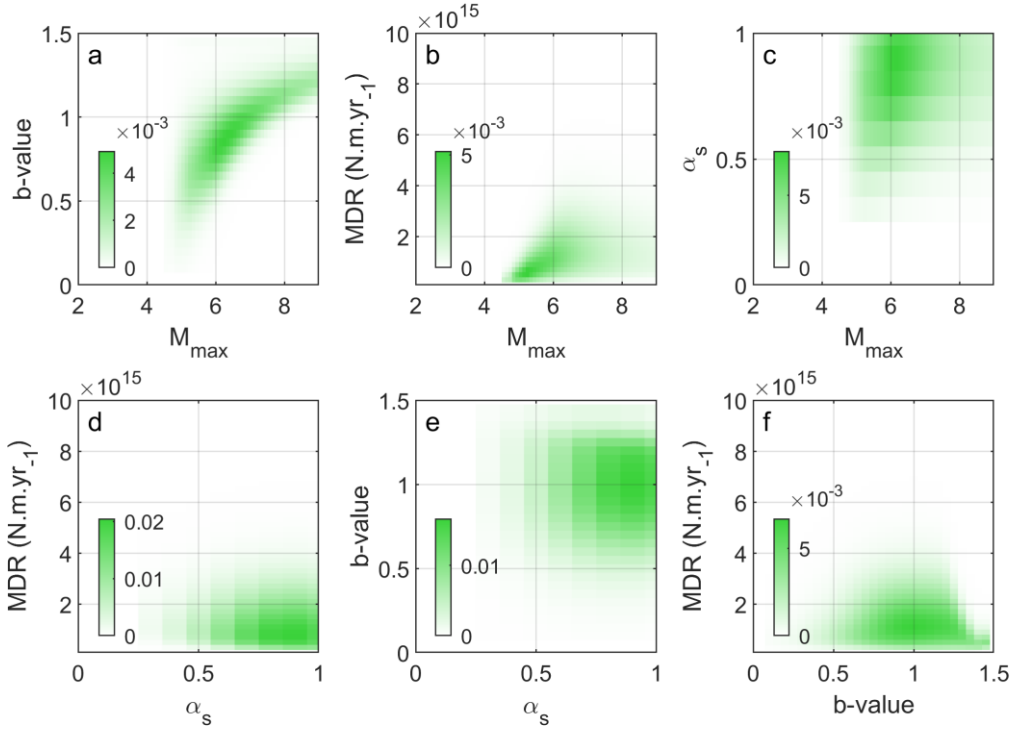

Figure S10: Correlation between correlation between M_{max}, the moment deficit rate (MDR), the b-value, and α_s, for the tapered model without the scaling law constraint.

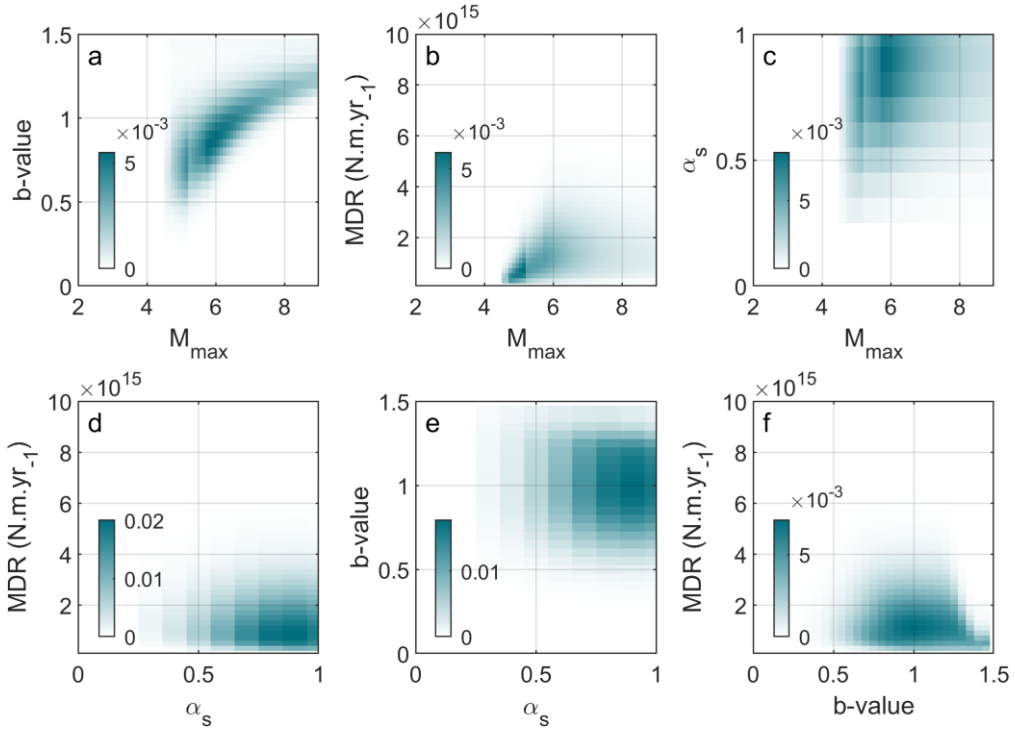

Figure S11: Correlation between correlation between M_{max}, the moment deficit rate (MDR), the b-value, and α_s, for the truncated model without the scaling law constraint.

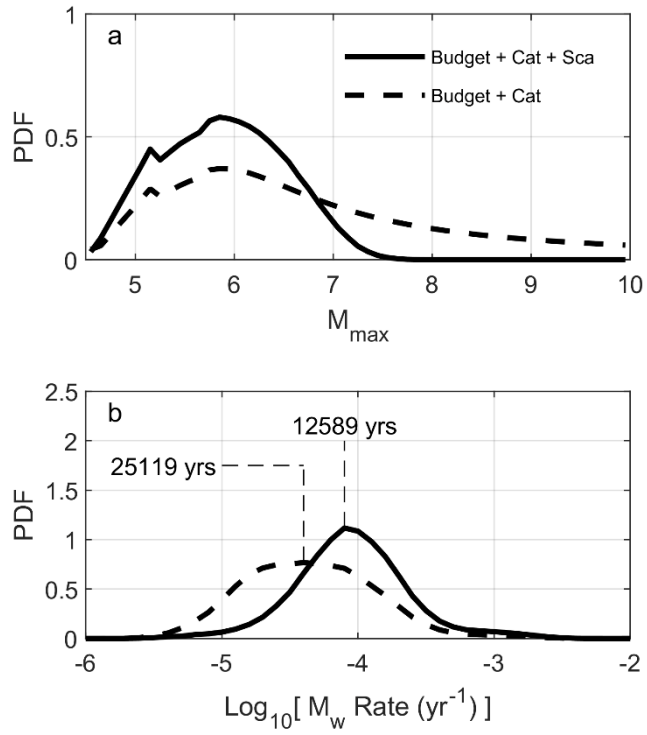

Figure S12: Same as Figure 5 but using mixture distribution from the tapered and truncated model. (a) Evolution of the marginal PDF of $M_{\max}$ when adding the moment-area scaling law constraint. (b) Same as (a) but for the marginal PDF of the recurrence time of events: $P(\tau \mid M_w = 5.9)$.

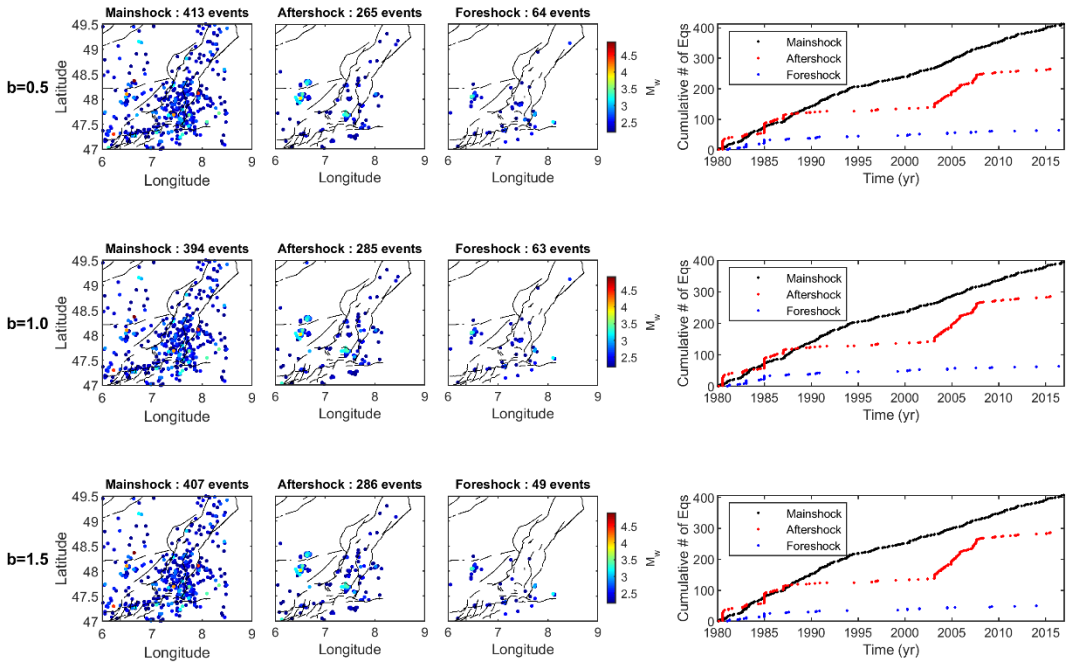

Figure S13: Results from the declustering method of Zaliapin and Ben-Zion (2013) for $M_w \geq 2.2$ events between 1980 and 2016, for different preset b-values.

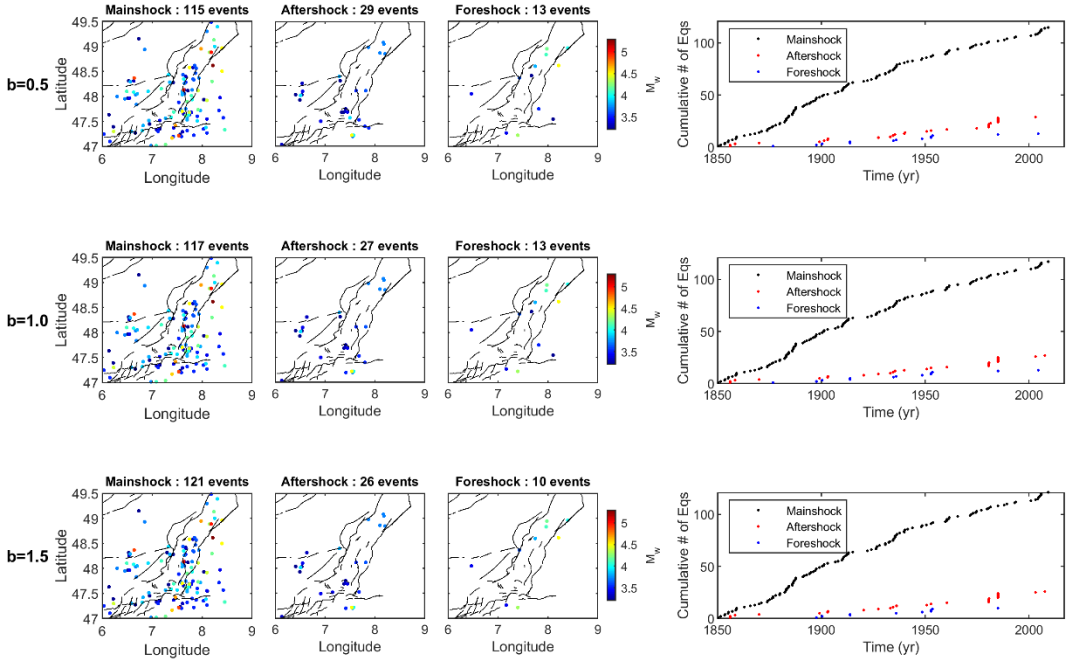

Figure S14: Results from the declustering method of Zaliapin and Ben-Zion (2013) for $M_w \geq 3.2$ events between 1850 and 2016, for different preset b-values.

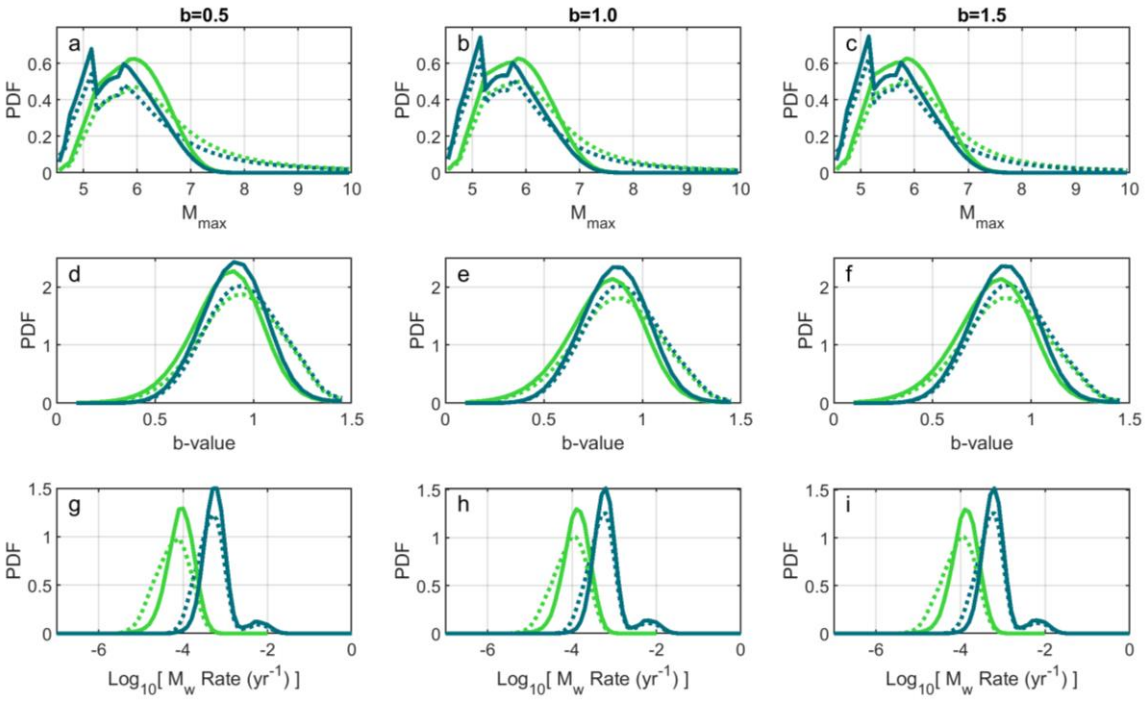

Figure S15: Results using the declustering method from Zaliapin and Ben-Zion (2013) instead of Marsan et al. (2017). In this scenario, no probabilities of events to be mainshocks are defined. (a), (b) and (c) M_{max} PDF. (d), (e) and (f) b-value PDF. (g), (h) and (i) $P(\tau \mid M_w = M_{Mode})$ PDF. (a), (d) and (g) correspond to the results using a declustering with b=0.5. (b), (e) and (f) correspond to the results using a declustering with b=1.5. (c), (f) and (i) correspond to the results using a declustering with b=1.5. Solid lines correspond to the results obtained with all constraints while the dotted lines only use the moment budget and earthquake catalog constraints. Green and blue lines indicate the results from the tapered and truncated models, respectively.

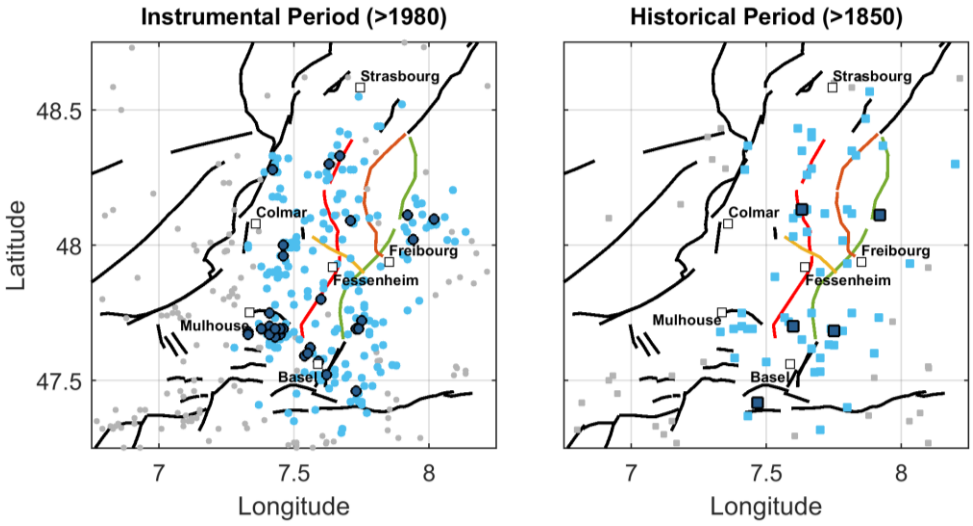

Figure S16: Earthquake selection for the instrumental (>1994) and historical (>1850) periods. Gray dots and squares indicate all earthquakes with $M_c = 2.2$ and 3.2 for the instrumental and historical catalogs, respectively. Light blue dots and squares indicate earthquakes within 20 km of the faults, taken into account for the seismogenic potential analysis in Figure S17 (Section 5.2). Dark blue dots and squares indicate $M_w > 2.7$ and 4.2 earthquakes taken into account for the seismogenic potential analysis.

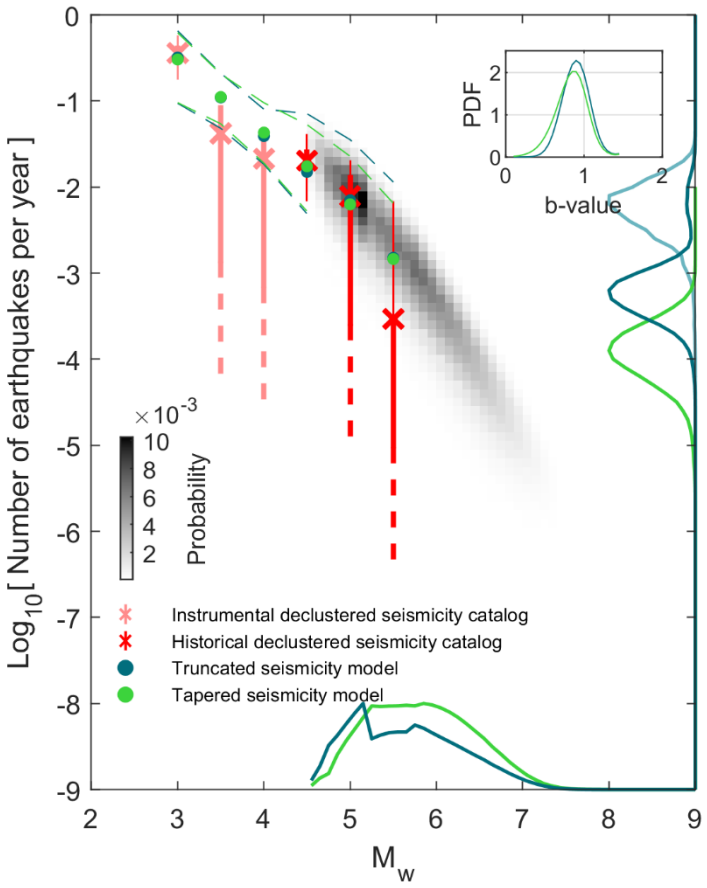

Figure S17: Seismogenic potential of the URG using all constraints, but taking events within 20 km of the faults, instead of 10 km as defined initially (Section 3.2). The rate of occurrence of historical and instrumental earthquakes, within their observation period, are indicated by red and pink crosses and error bars, respectively. The thick and thin error bars indicate the 15.9-84.1% (1-sigma) and 2.3-97.7% (2-sigma) quantiles of the MFDs. The dashed lines indicate that, within the 2500 catalog built to explore uncertainties, at least some catalogs do not have any events within the magnitude bin and observation period considered. The green and blue colors are associated with the tapered and truncated long-term seismicity models. Green and blue dots show the mean of the marginal PDF of the long-term seismicity. Dashed green and blue lines indicate the spread of the best 1% seismicity models. The marginal probabilities of M_{max}, $P_{M_{max}}$, are indicated by the solid lines on the M_w axis. They have been normalized so that their amplitude is equal to one instead of 0.58 and 0.75 for the tapered and truncated models respectively. The green and dark blue lines on the earthquake frequency axis indicate the probability of the rate of events, τ, with magnitude $M_w = M_{Mode}$, thus $P(\tau \mid M_w = M_{Mode})$, with M_{Mode}=5.9 and 5.2 for the tapered and truncated models, respectively. They have also been normalized and their peak were initially at 1.22 and 1.36 for the tapered and truncated models, respectively. It considers all magnitudes in the seismicity models and not only the recurrence rate of M_{max}. The solid light blue line on the earthquake frequency axis indicates $P(\tau_{max} \mid M_{max} = 5.2)$ (for the truncated seismicity model only) and is normalized so that its amplitude equals one instead of 1.37. The top-right inset shows the marginal probability of the b-value. Note that the seismicity MFDs in the figure are not in the cumulative form.

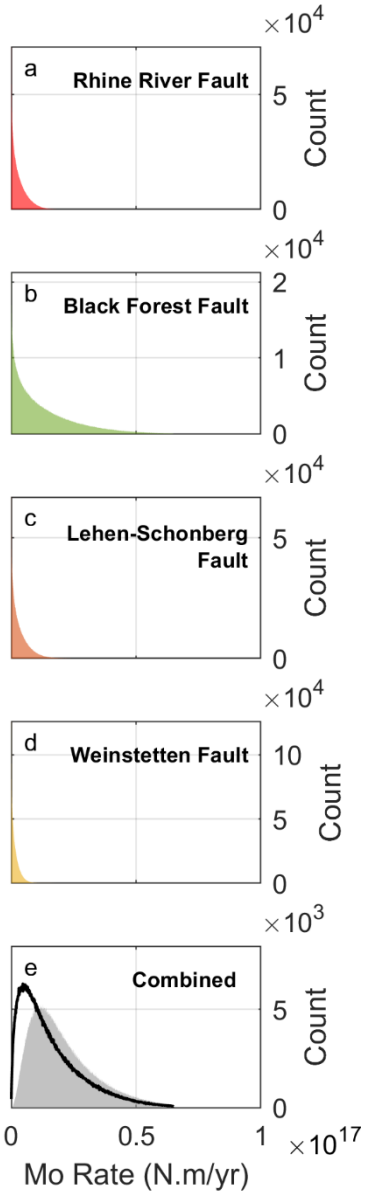

Figure S18: (a) to (e) Moment deficit rate PDF (expressed in counts) of each of the four faults considered (colors are indicative of the faults in the left panel of Figure 1), and of their combination (in grey), considering a strike-slip slip rate component equivalent to 4.8 times the dip-slip estimate, and assuming the Black Forest Fault maximum long-term vertical slip rate is 0.18 mm/yr (as proposed by Jomard et al., 2017) (Section 5.3). The black line in panel (e) indicates the combined MDR for the Rhine River and Black Forest faults alone, as proposed by Chartier et al. (2017).

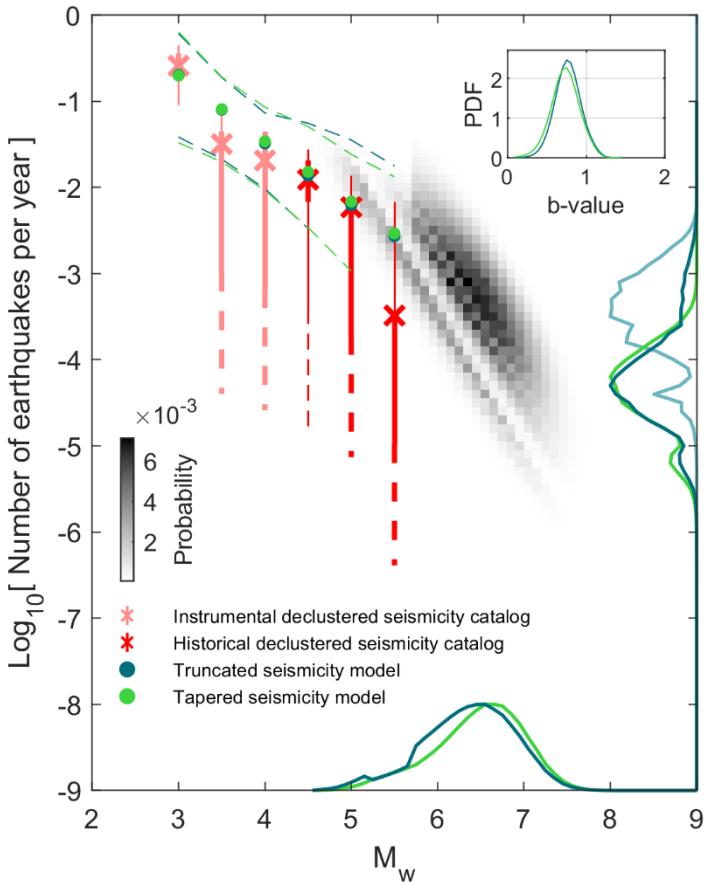

Figure S19: Seismogenic potential of the URG using all constraints, only taking into account the Rhine River and Black Forest faults (as in Chartier et al., 2017), considering a strike-slip slip rate component equivalent to 6.6 times the dip-slip estimate, and assuming the Black Forest Fault maximum long-term vertical slip rate is 0.18 mm/yr (as proposed by Jomard et al., 2017) (Section 5.3). Leonard et al. (2010) strike-slip moment-area scaling law is used here for the scaling law constraint, even though it is very similar to the dip-slip version. The rate of occurrence of historical and instrumental earthquakes, within their observation period, are indicated by red and pink crosses and error bars, respectively. The thick and thin error bars indicate the 15.9-84.1% (1-sigma) and 2.3-97.7% (2-sigma) quantiles of the MFDs. The dashed lines indicate that, within the 2500 catalog built to explore uncertainties, at least some catalogs do not have any events within the magnitude bin and observation period considered. The green and blue colors are associated with the tapered and truncated long-term seismicity models. Green and blue dots show the mean of the marginal PDF of the long-term seismicity. Dashed green and blue lines indicate the spread of the best 1% seismicity models. The marginal probabilities of M_{max}, $P_{M_{max}}$, are indicated by solid lines on the M_w axis. They have been normalized so that their amplitude is equal to one instead of 0.80 and 0.75 for the tapered and truncated models, respectively. The dotted lines on the earthquake frequency axis indicate the probability of the rate of events, τ, with magnitude $M_w = M_{Mode}$, thus $P(\tau \mid M_w = M_{Mode})$, with M_{Mode}=6.7 and 6.6 for the tapered and truncated models, respectively. It considers all magnitudes in the seismicity models and not only the recurrence rate of M_{max}. They have also been normalized and their peaks were initially at 0.94 for both the tapered and truncated models. The solid blue line on the earthquake frequency axis indicates $P(\tau_{max} \mid M_{max} = 6.6)$ (for the truncated seismicity model only) and is normalized so that its amplitude equals one instead of 0.87. The top-right inset shows the marginal probability of the b-value. Note that the seismicity MFDs in the figure are not in the cumulative form.

Bibliography

Blanpied, M. L., Lockner, D. A., and Byedee, D.: Frictional slip of granite at hydrothermal conditions, J. Geophys. Res., 100, no. B7, 13,045-13,064, https://doi.org/10.1029/95JB00862, 1995.

Chartier, T., Scotti, O., Lyon-Caen, H., and Boiselet, A.: Methodology for earthquake rupture rate estimates of fault networks: example for the western Corinth rift, Greece, Nat. Hazards Earth Syst. Sci., 17, no. 10, 1857–1869, https://doi.org/10.5194/nhess-17-1857-2017, 2017.

Churchill, R. M., Werner, M. J., Biggs, J., and Fagereng, Å.: Afterslip Moment Scaling and Variability From a Global Compilation of Estimates, J. Geophys. Res. Solid Earth, 127, no. 4, https://doi.org/10.1029/2021JB023897, 2022.

Daniel, G., Marsan, D., and Bouchon, M.: Earthquake triggering in southern Iceland following the June 2000 Ms 6.6 doublet, J. Geophys. Res., 113, no. B5, B05310, https://doi.org/10.1029/2007JB005107, 2008.

Drouet, S., Ameri, G., Le Dortz, K., Secanell, R., and Senfaute, G.: A probabilistic seismic hazard map for the metropolitan France, Bull. Earthq. Eng., 18, no. 5, 1865–1898, https://doi.org/10.1007/s10518-020-00790-7, 2020.

Guillou-Frottier, L., Carrė, C., Bourgine, B., Bouchot, V., and Genter, A.: Structure of hydrothermal convection in the Upper Rhine Graben as inferred from corrected temperature data and basin-scale numerical models, J. Volcanol. Geotherm. Res., 256, 29–49, https://doi.org/10.1016/j.jvolgeores.2013.02.008, 2013.

Jara, J., Socquet, A., Marsan, D., and Bouchon, M.: Long-term interactions between intermediate depth and shallow seismicity in north Chile subduction zone, Geophys. Res. Lett. 44, no. 18, 9283–9292, https://doi.org/10.1002/2017GL075029, 2017.

Jomard, H., Cushing, E. M., Palumbo, L., Baize, S., David, C., and Chartier, T.: Transposing an active fault database into a seismic hazard fault model for nuclear facilities – Part 1: Building a database of potentially active faults (BDFA) for metropolitan France, Nat. Hazards Earth Syst. Sci., 17, no. 9, 1573–1584, https://doi.org/10.5194/nhess-17-1573-2017, 2017.

Marsan, D., Bouchon, M., Gardonio, B., Perfettini, H., Socquet, A. and B., Enescu, A.: Change in seismicity along the Japan trench, 1990-2011, and its relationship with seismic coupling, J. Geophys. Res. Solid Earth, 122, no. 6, 4645–4659, https://doi.org/10.1002/2016JB013715, 2017.

Ogata, Y.: Space-Time Point-Process Models for Earthquake Occurrences, Ann. Inst. Stat. Math., 50, no. 2, 379–402, https://doi.org/10.1023/A:1003403601725, 1998.

Ogata, Y., and Katsura, K.: Analysis of temporal and spatial heterogeneity of magnitude frequency distribution inferred from earthquake catalogues, Geophys. J. Int., 113, no. 3, 727–738, https://doi.org/10.1111/j.1365-246X.1993.tb04663.x, 1993.

Wiemer, S., and Wyss, M.: Minimum magnitude of completeness in earthquake catalogs: Examples from Alaska, the Western United States, and Japan, Bull. Seismol. Soc. Am., 90, no. 4, 859–869, https://doi.org/10.1785/0119990114, 2000.

Zaliapin, I., and Ben-Zion, Y.: Earthquake clusters in southern California I: Identification and stability, J. Geophys. Res. Solid Earth, 118, no. 6, 2847–2864, https://doi.org/10.1002/jgrb.50179, 2013.